



Cite this: *Mater. Adv.*, 2021, 2, 736

The hydrogen storage properties of $\text{MgH}_2\text{--Fe}_7\text{S}_8$ composites

Ying Cheng,^{†a} Jia Bi^{†b} and Wei Zhang   *^b

Nanostructured Fe_7S_8 was successfully synthesized and its catalytic effect on hydrogen absorption/desorption performance of MgH_2 is systematically discussed. The $\text{MgH}_2 + 16.7$ wt% Fe_7S_8 composite prepared by ball-milling method offers a striking catalytic activity for hydrogenation kinetics, and also reduces the initial decomposition temperature for MgH_2 . The composite of $\text{MgH}_2\text{--Fe}_7\text{S}_8$ can absorb 4.000 wt% of hydrogen within 1800 s at 473 K, which is about twice that of pristine MgH_2 (1.847 wt%) under the same conditions. The onset hydrogen release temperature of Fe_7S_8 -modified MgH_2 is 420 K, which is 290 K lower than that of additive-free MgH_2 (710 K). Meanwhile, the doped sample could release 4.403 wt% of hydrogen within 1800 s at 623 K as compared to 2.479 wt% of hydrogen by MgH_2 . The activation energy for $\text{MgH}_2\text{--Fe}_7\text{S}_8$ is about $130.0 \text{ kJ mol}^{-1}$, approximately 36 kJ mol^{-1} lower than that of MgH_2 . The hydriding process of $\text{MgH}_2 + 16.7$ wt% Fe_7S_8 follows the nucleation and growth mechanism. The prominent hydrogen storage performances are related to the reactions between MgH_2 and Fe_7S_8 . The newly formed MgS and Fe in the ball-milling process present a co-catalytic effect on the hydrogen storage performance of MgH_2 .

Received 20th October 2020,
Accepted 19th November 2020

DOI: 10.1039/d0ma00818d

rsc.li/materials-advances

1. Introduction

The global environmental issues related to the excessive emission of greenhouse gases and burning of fossil materials have driven us to center our attention on alternative energy sources that can be extensively developed and widely used.^{1–4} Meanwhile, hydrogen energy is deemed as one of the most potential and ideal energy alternatives on account of its high energy density and clean and environmentally friendly nature.^{5–8} However, the practical application and popularization of hydrogen is still hindered by numerous complicated technical hurdles. In recent years, solid-state storage materials have been receiving worldwide attention as ideal hydrogen storage media. Among them, magnesium hydride (MgH_2), which has a high hydrogen storage capacity, excellent reversibility and abundant availability, is regarded as one of the most marvelous candidates for potential hydrogen storage.^{9–12} Unfortunately, the widespread practical application of MgH_2 is retarded by sluggish dynamic performance and high thermodynamic operating temperature.

Various attempts covering mechanical alloying,^{13,14} nano-structuring,¹⁵ and catalyst doping^{16–20} have been made by numerous

groups to enhance the thermodynamic and hydrogen absorption and desorption properties. Among the above-mentioned modified systems, doping MgH_2 with catalysts has been considered as an efficient way to boost the properties of MgH_2 .^{21–23} Especially, the transition metal iron (Fe) and its compounds have attracted considerable interest due to their pronounced catalytic effect on MgH_2 . Yan *et al.*¹⁵ observed a lower onset dehydrogenation temperature for the $\text{MgH}_2\text{--}10$ wt% FeB/CNTs composite; the modified composites could start to release hydrogen at about 196 °C and absorb 6.2 wt% of H_2 at 150 °C within 10 min. Chen *et al.*²⁴ found that doping MgH_2 with 5 wt% Fe nanosheets reduced the onset desorption temperature, and hydrogen could be released at 182.1 °C and absorbed at 75 °C by the composite. Gattia *et al.*²⁵ reported that Fe and its oxides are suitable catalysts for hydrogen storage as they drastically speed up the reaction kinetics.

In addition to iron and its compounds, sulfide compounds also showed remarkable catalytic activities for the improvement of sorption kinetics and thermodynamic properties of MgH_2 . Jia *et al.*²⁶ discovered that MgH_2 with 16.7 wt% of MoS_2 additive showed outstanding hydrogenation/dehydrogenation properties and the hydrogenation activation energy of the modified composites was determined to be $87.19 \pm 4.48 \text{ kJ mol}^{-1}$, lower than that of the pure MgH_2 ($111.03 \pm 3.41 \text{ kJ mol}^{-1}$). WS_2 was also found to promote the hydrogenation/dehydrogenation behavior of MgH_2 by Wang *et al.*²⁷ Our previous work reported that the hydrogen intake/uptake performance of MgH_2 was greatly influenced by nano-structured polysulfides containing iron (Fe_3S_4 and FeS_2).^{28,29}

^a Hebei University of Environmental Engineering, Qinhuangdao, 066102, P. R. China

^b Hebei Key Laboratory of Applied Chemistry, School of Environmental and Chemical Engineering, Yanshan University, Qinhuangdao 066004, P. R. China.
E-mail: zhangweihh@ysu.edu.cn; Tel: +86-335-8387744

† Both authors contributed equally to this work.



The polysulfide containing iron ion is a kind of compound in polyvalent states, which can be approximately considered by the compound of ferrous sulfide and iron sulfide. Multi-valent catalysts also showed great potential in enhancing de-/hydrogenation kinetics of MgH_2 as reported by Xie and co-workers.³⁰ Meanwhile, the excellent hydrogen storage behavior of MgH_2 might be related to the unstable Fe^{2+} . Fe_7S_8 is also a polysulfide containing iron; multi-valent and unstable Fe^{2+} exist in Fe_7S_8 , which might contribute to the enhancement of the hydrogen storage capacity of MgH_2 .

Given the encouraging results mentioned above, in this work, Fe_7S_8 was successfully synthesized and its catalytic effectiveness toward hydrogen adsorption/desorption of MgH_2 was systematically investigated. Besides, the corresponding catalytic mechanism of Fe_7S_8 to the enhancement of hydrogen properties of the pristine MgH_2 was also presented based on the information reflected by hydrogen absorption/desorption kinetics, phase compositions and microstructure observations.

2. Experimental

2.1 Synthesis of Fe_7S_8

1 mmol $\text{FeSO}_4 \cdot 7\text{H}_2\text{O}$ and 2 mmol thiourea were added to a solvent composed of triethylenetetramine and deionized water (the ratio of the components of the solvent was 1:2) and stirred for 1 h by magnetic stirring until the solution was homogenized. The solution was then transferred into a Teflon autoclave and maintained at 140 °C for 24 h. After cooling down to room temperature naturally, the precipitate was gathered by centrifugation and washed with distilled water and absolute alcohol several times. The obtained precipitate was dried in a vacuum oven at 80 °C for 6 h. The precursor $[\text{Fe}_{18}\text{S}_{25}](\text{TETA})_{14}$ was finally prepared.

0.1 g precursor $[\text{Fe}_{18}\text{S}_{25}](\text{TETA})_{14}$ and 15 ml oleylamine were added into a boiling flask and promptly heated to 90 °C in a vacuum atmosphere. To protect the sample from oxidation, argon was introduced into the boiling flask as a protective gas after the vacuum was stopped. The sample was then quickly heated to 260 °C and kept warm for 8 h. After the reaction was complete and the temperature of the boiling flask decreased to room temperature, extra 40 ml alcohol was introduced into the flask under mechanical stirring for about 10 min and the solution was further aged for 2 h. Fe_7S_8 was successfully synthesized and could be separated after the aged solution was centrifuged and washed with absolute alcohol.

2.2 Synthesis of $\text{MgH}_2\text{-Fe}_7\text{S}_8$ composites

MgH_2 was synthesized by the method of hydrogen combustion from commercial magnesium powder. Magnesium was hydrogenated at 400 °C with a hydrogen pressure of 4 MPa for 10 h. The obtained powder was then ball-milled at 350 rpm for 2 h. The target MgH_2 was successfully prepared after hydrogenating the sample one more time at 400 °C under 4 MPa hydrogen pressure for 10 h.

$\text{MgH}_2\text{-Fe}_7\text{S}_8$ composite was synthesized through the ball-milling method by mechanical milling of MgH_2 and Fe_7S_8 with

a weight ratio of 5:1. To reduce the increasing temperature, the milling process was launched at a speed of 350 rpm and ball-milled in one direction for 0.5 h and paused for about 0.25 h, unceasingly starting in another direction for 0.5 h. The ball-to-sample weight ratio was 20:1. To prevent the sample from oxygen and vapor, all samples were handled in an air-filled glove box.

2.3 Characterization

X-ray diffraction (XRD) was performed on a SmartLab high-resolution X-ray diffractometer (made by Rigaku Company) with $\text{Cu K}\alpha$ radiation at 40 kV, 40 mA. The scanning speed was 4° min⁻¹ in the range of 10° to 80°. Scanning electron microscopy (SEM) was employed to observe the microstructure and morphology of the formed sample. The hydrogen absorption/desorption behavior in relation to temperature for the composite of $\text{MgH}_2\text{-Fe}_7\text{S}_8$ and non-additive MgH_2 was determined in a pressure-composition-temperature (PCT) apparatus. The sample was gradually heated from room temperature to the set temperature, which was kept constant during the whole experiment. Temperature-programmed-desorption (TPD) was used to investigate the initial desorption temperature for the composite of $\text{MgH}_2\text{-Fe}_7\text{S}_8$ and MgH_2 free-additive. All the tested composites were heated from room temperature to 770 K at a heating rate of 10 K min⁻¹. Differential scanning calorimetry (DSC) was performed from 200 K to 770 K at various heating rates: 5 K min⁻¹, 10 K min⁻¹, 15 K min⁻¹, and 20 K min⁻¹.

3. Results and discussion

3.1 Characteristics of the prepared nano-structured Fe_7S_8

XRD pattern of the as-synthesized Fe_7S_8 in Fig. 1a exhibits dominant diffraction peaks at $2\theta = 29.9^\circ, 33.8^\circ, 43.9^\circ, 53.1^\circ, 57.3^\circ, 64.8^\circ$, and 71.2° matching well with the Fe_7S_8 phase, in accordance with the data reported in JCPDS PDF 33-0664. As can be seen from Fig. 1b, the prepared sample presents the morphology of two-dimensional hexagonal sheets with a thickness of approximately 20 nm and a diameter of around 250 nm. Based on XRD and SEM results, nano-structured Fe_7S_8 was successfully fabricated.

3.2 Catalytic effectiveness of the fabricated Fe_7S_8 for the dehydrogenation/hydrogenation kinetics of MgH_2

The catalytic role of the as-synthesized Fe_7S_8 in the dehydrogenation/hydrogenation kinetics of MgH_2 was studied by using TPD isothermal dehydrogenation/hydrogenation measurements. The TPD curves of MgH_2 and $\text{MgH}_2 + 16.7$ wt% Fe_7S_8 composite at a heating rate of 10 K min⁻¹ are shown in Fig. 2. As observed, the Fe_7S_8 doped MgH_2 sample shows a striking effect of reducing the onset desorption temperature of MgH_2 . The prepared MgH_2 commences to release hydrogen at approximately 710 K, whereas the onset desorption temperature for Fe_7S_8 -modified MgH_2 presents a remarkable decrease to 420 K, which is 290 K lower than that of additive-free MgH_2 . As for the pristine MgH_2 , the full desorption capacity is about 4.45 wt%. After introducing nano- Fe_7S_8 into MgH_2 , the desorbed content is increased and the maximum yield for the desorption process



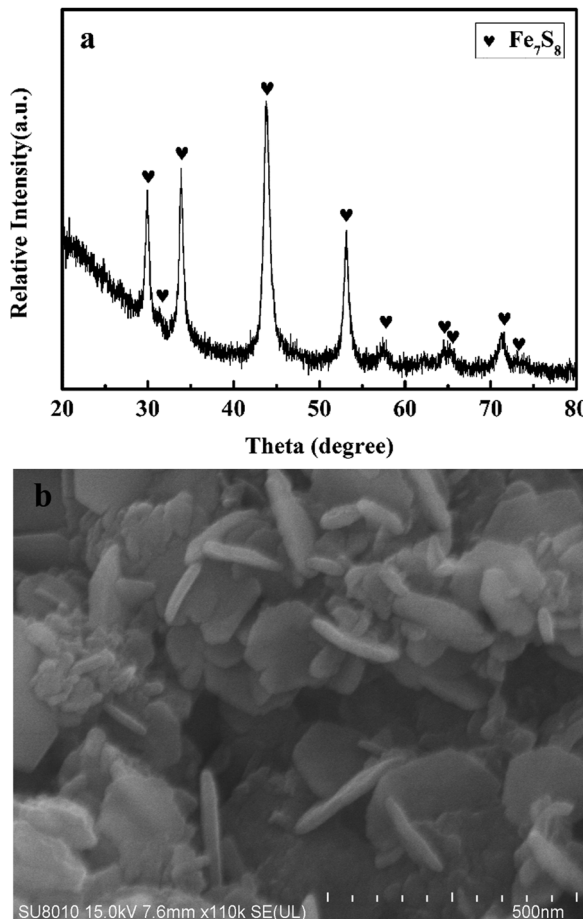


Fig. 1 (a) XRD pattern of the as-synthesized Fe_7S_8 (b) SEM image of the as-synthesized Fe_7S_8 .

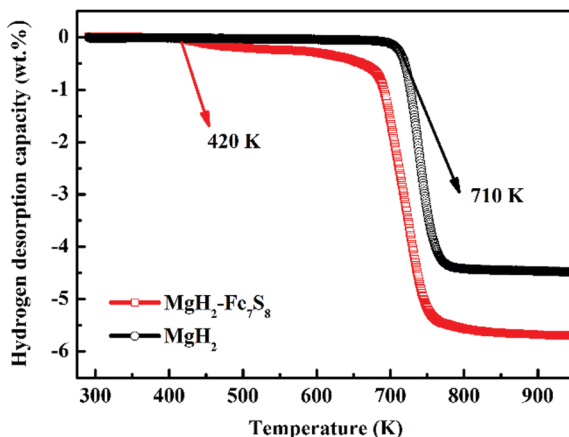


Fig. 2 Thermal decomposition curves of MgH_2 and $\text{MgH}_2 + 16.7 \text{ wt\% Fe}_7\text{S}_8$ composite.

is nearly 5.72 wt%. Based on TPD measurements, the lower initial desorption temperature and the maximum desorption yield reveal that the introduced nano- Fe_7S_8 into MgH_2 could successfully boost the desorption properties of MgH_2 .

Isothermal dehydrogenation experiments were conducted at 623 K to further compare the effect of the doped Fe_7S_8 on the desorption kinetics process in MgH_2 ; the relative curves for MgH_2 with and without additives in the desorption process are presented in Fig. 3. It is evident that with the increase in temperature, the hydrogen desorption properties of MgH_2 and $\text{MgH}_2 + 16.7 \text{ wt\% Fe}_7\text{S}_8$ are enhanced. $\text{MgH}_2 + 16.7 \text{ wt\% Fe}_7\text{S}_8$ composite exhibits much faster kinetics than that of pristine MgH_2 . The $\text{MgH}_2 + 16.7 \text{ wt\% Fe}_7\text{S}_8$ sample could release 1.515 wt% H_2 in 1800 s at 573 K. In contrast, the pure MgH_2 only liberated 0.250 wt% H_2 in the same time period. When the temperature increases to 623 K, the additive-free MgH_2 , which could only desorb 2.479 wt% of hydrogen in 1800 s at 623 K, shows worse desorption properties than the doped sample. $\text{MgH}_2 + 16.7 \text{ wt\% Fe}_7\text{S}_8$ composite could liberate 4.403 wt% of hydrogen within 1800 s under identical conditions. As compared to non-additive MgH_2 , the dopant Fe_7S_8 promotes the dehydrogenation kinetics.

The Kissinger's method³¹ was performed to further understand the enhanced dehydrogenation process for MgH_2 and $\text{MgH}_2-\text{Fe}_7\text{S}_8$ composites; the apparent activation energy (E_a) of those two composites were estimated by the Arrhenius equation described as below:

$$\frac{d[\ln(\alpha/T_m^2)]}{d(1/T_m)} = \frac{-E_a}{R}$$

where α is the heating rate (K min^{-1}), T_m is the peak temperature for the maximum desorption rate (K), and R is the gas constant of $8.314 \text{ J (mol}^{-1} \text{ K}^{-1}\text{)}$. Fig. 4a and b display DSC curves of MgH_2 and $\text{MgH}_2-\text{Fe}_7\text{S}_8$ composites, respectively, at various heating rates. From the slope of the fitted line in Fig. 4c, the slope for the two samples were obtained as -19.95 and -15.64 , while the corresponding apparent activation energy E_a for MgH_2 was approximately $165.9 \text{ kJ mol}^{-1}$. It can be noticed that the apparent activation energy E_a of $\text{MgH}_2-\text{Fe}_7\text{S}_8$ was decreased to $130.0 \text{ kJ mol}^{-1}$, which is lower by about 36 kJ mol^{-1} than that of MgH_2 . The reduced apparent activation energy demonstrated above gives

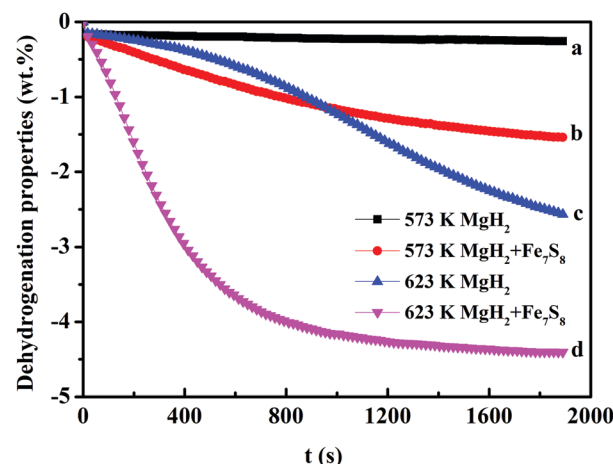


Fig. 3 Dehydrogenation properties of MgH_2 and $\text{MgH}_2 + 16.7 \text{ wt\% Fe}_7\text{S}_8$ composite at 573 K, 623 K.



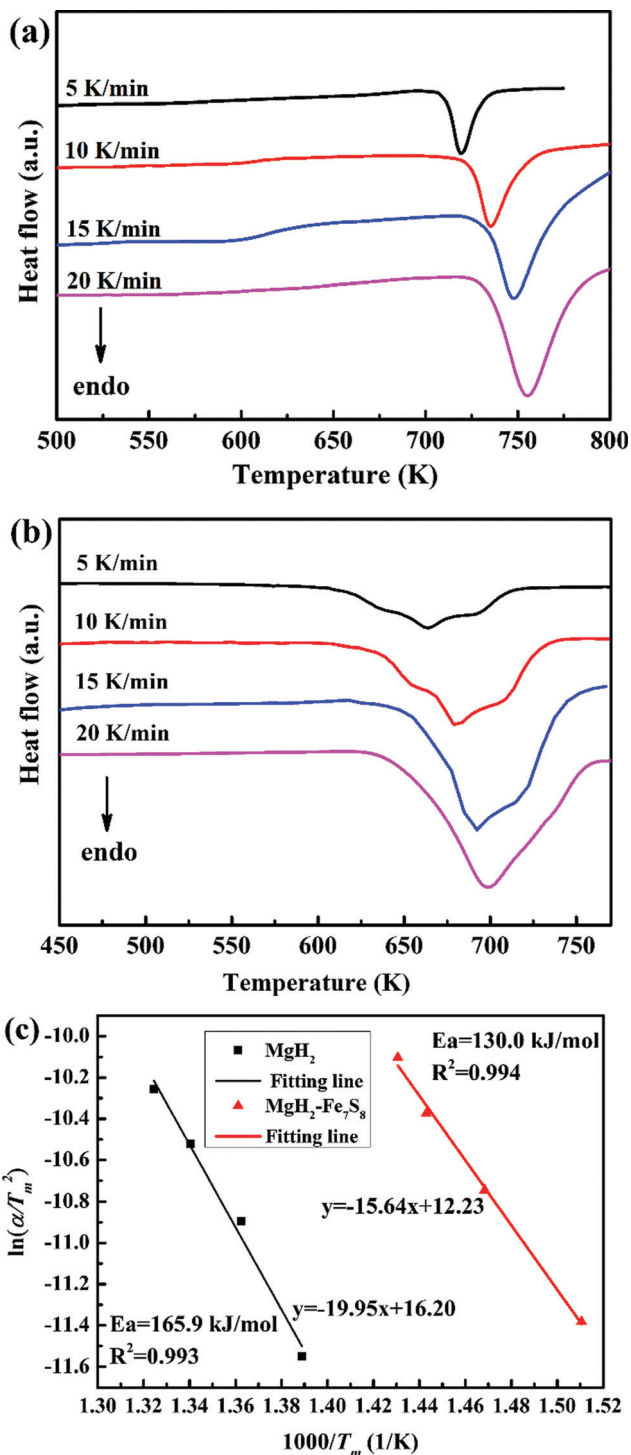


Fig. 4 DSC curves of (a) pure MgH_2 and (b) $\text{MgH}_2 + 16.7 \text{ wt\% Fe}_7\text{S}_8$ composites with a heating rate of 5 K min^{-1} , 10 K min^{-1} , 15 K min^{-1} , 20 K min^{-1} . (c) The corresponding Kissinger plots for the hydrogen desorption reaction for MgH_2 and $\text{MgH}_2 + 16.7 \text{ wt\% Fe}_7\text{S}_8$ composites at various heating rates.

the indication that the dopant Fe_7S_8 contributes to decreasing the energy barrier during the desorption process of MgH_2 , which is directly responsible for the superior improvement of the dehydrogenation properties. In a recent literature,²⁵ activation energies for milled $\text{MgH}_2 + 5 \text{ wt\% Fe}$, $\text{MgH}_2 + 5 \text{ wt\% Fe}_2\text{O}_3$ and $\text{MgH}_2 + 5 \text{ wt\%}$

Fe_3O_4 calculated using the Kissinger plot were $220.69 \text{ kJ mol}^{-1}$, $231.90 \text{ kJ mol}^{-1}$ and $304.45 \text{ kJ mol}^{-1}$, respectively, which indicates that the addition of Fe_7S_8 may show superior catalytic effect compared to that of some other additives.

In addition to the hydrogen desorption behavior, the modified impact of Fe_7S_8 on the hydrogen uptake performance on MgH_2 was also investigated by reabsorbing the dehydrogenated MgH_2 and $\text{MgH}_2\text{-Fe}_7\text{S}_8$ composites under 3 MPa of H_2 . Fig. 5 presents the hydrogenation curves of MgH_2 and $\text{MgH}_2\text{-Fe}_7\text{S}_8$ composite at 473 K and 523 K, respectively. It can be clearly seen that the dehydrogenated MgH_2 sample only absorbs 1.847 wt% of hydrogen within 1800 s at 473 K, whereas the dehydrogenated MgH_2 catalyzed by Fe_7S_8 composite shows higher hydrogen absorption ability under the same conditions, with an absorption capacity of 4.000 wt%. When the temperature sharply increases to 523 K, the hydrogen absorption ability of both dehydrogenated $\text{MgH}_2\text{-Fe}_7\text{S}_8$ composite and additive-free MgH_2 presents an obvious rise. The amount of hydrogen uptake increases to 3.915 wt% for pristine MgH_2 within 1800 s, while that of the Fe_7S_8 doped composite reaches 4.804 wt%.

The hydrogenation mechanism can usually be explained by comparing the hydrogen absorption rate curves with the rate equations for $\text{MgH}_2 + 16.7 \text{ wt\% Fe}_7\text{S}_8$ and MgH_2 composites. The Avrami-Erofeev equation, eqn (2), is usually employed to fit the hydrogenation absorption process, which gives a strong idea for the nucleation and growth processes.

$$\alpha = 1 - \exp(-kt^m)$$

where α is the reacted fraction, k is the rate constant, and m is the order of the reaction. Fig. 6 shows the fitted hydrogenation kinetic curves of MgH_2 and $\text{MgH}_2 + 16.7 \text{ wt\% Fe}_7\text{S}_8$ composites at 523 K. It is obvious that there is a great difference between the fitted curve and the normalized curve for MgH_2 without additives. However, this similar phenomenon does not appear in the composite of $\text{MgH}_2\text{-Fe}_7\text{S}_8$, which is consistent with the experimental data. The fitted curves in Fig. 6 demonstrate that the reaction mechanism of $\text{MgH}_2\text{-Fe}_7\text{S}_8$ composite conforms to nucleation and growth processes. Besides, m represents the

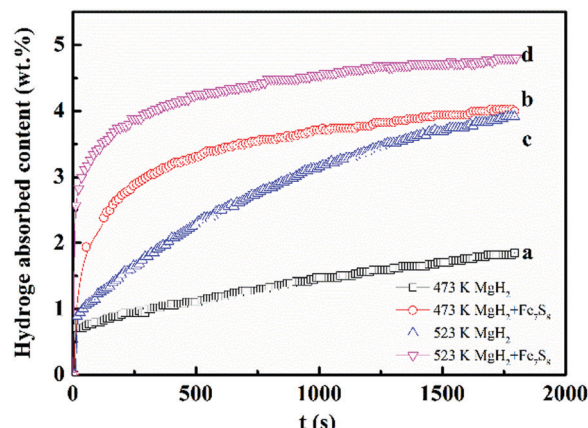


Fig. 5 Hydrogenation properties of (a) MgH_2 at 473 K; (b) $\text{MgH}_2 + 16.7 \text{ wt\% Fe}_7\text{S}_8$ composite at 473 K; (c) MgH_2 at 523 K; (d) $\text{MgH}_2 + 16.7 \text{ wt\% Fe}_7\text{S}_8$ composite at 523 K.

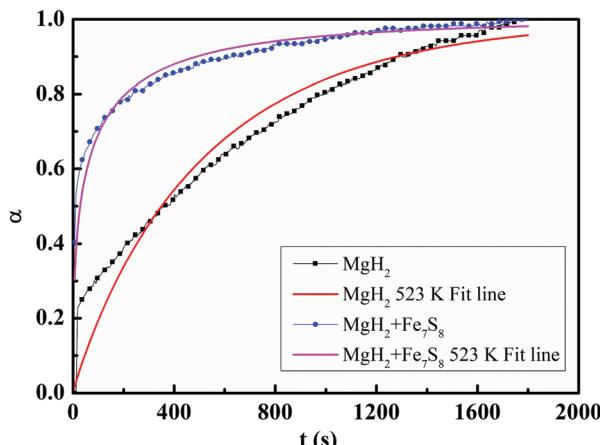


Fig. 6 Fitted hydrogenation kinetic curves of MgH_2 and $\text{MgH}_2 + 16.7$ wt% Fe_7S_8 composites at 523 K under the pressure of 3 MPa.

order of reaction; the rate-controlling steps for the hydrogen uptake process are connected with the value of m . It has been reported that the values of m for the one-dimensional diffusion process and the three-dimensional interfacial reaction are assigned as 0.620 and 1.070, respectively.³² As for MgH_2 without the catalyst, m is 0.9265 at 523 K, which is pretty close to 1.070. For the doped $\text{MgH}_2\text{-Fe}_7\text{S}_8$ composite, the value of m was 0.4212, which approaches 0.620. Therefore, the rate-controlling steps of MgH_2 during the hydrogenation process changes from the three-dimensional interfacial reaction to the one-dimensional diffusion process, which is relevant to the addition of Fe_7S_8 .

3.3 Structural characterization and catalytic effect mechanism of $\text{MgH}_2\text{-Fe}_7\text{S}_8$ composite

Fig. 7 presents SEM images of MgH_2 and $\text{MgH}_2\text{-Fe}_7\text{S}_8$ composite after the re-hydrogenation process. It is obvious that the particle size of pristine MgH_2 is much bigger than that of $\text{MgH}_2\text{-Fe}_7\text{S}_8$ composite; some of the particles in pristine MgH_2 are aggregated and inhomogeneous. The particles in the Fe_7S_8 added MgH_2 have a loose structure and are highly dispersed, while the particles of additive-free MgH_2 aggregate into large clusters and become tough. Xie *et al.*³³ and Varin *et al.*³⁴ reported that the decreased particle size and loose structure could boost the rates of dehydrogenation-hydrogenation, which indicates that the

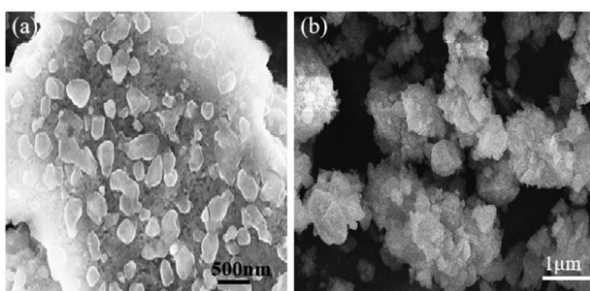
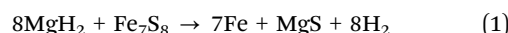


Fig. 7 SEM images of (a) MgH_2 , (b) $\text{MgH}_2\text{-Fe}_7\text{S}_8$ composite after the re-hydrogenation process.

added Fe_7S_8 can not only help to decrease the particle size but also serve as an inhibitor to limit the formation of large clusters and result in favourable hydrogen kinetics.

To further elaborate on the catalytic mechanism related to the striking hydrogen absorption/desorption kinetics and thermodynamic properties of $\text{MgH}_2\text{-Fe}_7\text{S}_8$ composite, XRD analysis was employed to characterize the phase structure of the doped composite at different stages. Fig. 8 shows the XRD patterns of $\text{MgH}_2\text{-Fe}_7\text{S}_8$ composites that were collected at the ball-milling and de/hydrogenation stages. In the XRD pattern of the composite at the ball-milling stage, the main diffraction peak assigned to MgH_2 appears accompanied by some new phases of Mg_2FeH_6 , MgS , and Fe . In the XRD pattern of the composite at the hydrogenation stage, all the diffraction peaks are very intense due to hydrogenation. After the re-hydrogenation procedure, the major diffraction peaks assigned to Fe , Mg_2FeH_6 and MgS are still present. The appearance of new phases of Mg_2FeH_6 , MgS and Fe indicates the reaction of MgH_2 and Fe_7S_8 during the ball-milling/re-hydrogenation stage. The reactions can be summarized as follows:



To confirm the possibility of the reaction between MgH_2 and Fe_7S_8 , the total change ΔG^θ was calculated. The standard $\Delta_f H_m^\theta$ for MgH_2 , Fe_7S_8 , and MgS is -75.3 , -824.2 , and -346 kJ mol $^{-1}$, and $\Delta_f G_m^\theta$ are -35.9 , -742.2 , and -341.8 kJ mol $^{-1}$, respectively. The total change ΔG^θ for reaction (1) is -1705.0 kJ mol $^{-1}$, whereas ΔG^θ for MgH_2 is -35.9 kJ mol $^{-1}$; this confirms the possibility of occurrence of reaction (1) from the thermodynamic potentials, and the dopant Fe_7S_8 is conducive to the hydrogen absorption/desorption process.

In the XRD pattern of the composite at the dehydrogenation stage, the dominant diffraction peak belongs to Mg , implying that Mg_2FeH_6 and MgH_2 produced in the hydrogenation process

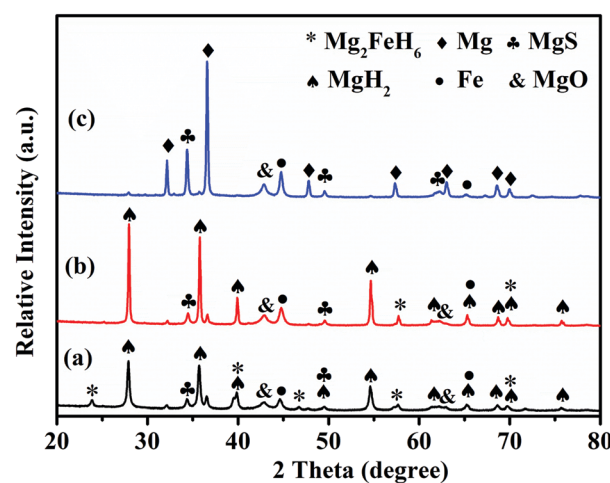


Fig. 8 XRD patterns of $\text{MgH}_2\text{-Fe}_7\text{S}_8$ composites at the (a) ball-milling (b) hydrogenation (c) dehydrogenation stages.



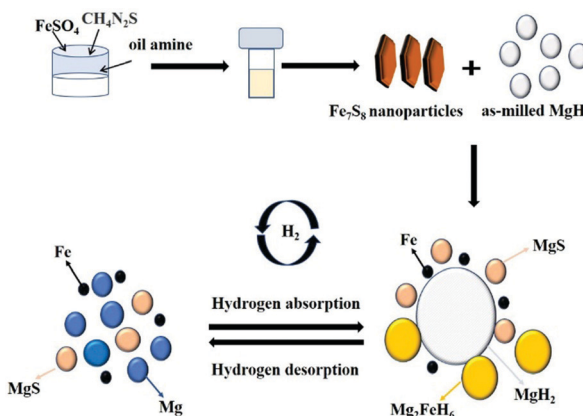


Fig. 9 Schematic diagram of the catalytic mechanism of Fe_7S_8 during the hydrogenation/dehydrogenation processes on MgH_2 .

have completely decomposed. Some weak peaks corresponding to MgO are found during the whole stage, which is ascribed to the oxidation of Mg in the test operation process. The existing equation in the hydrogen release stage is as follows:



The formation of the intermediate phase of Mg_2FeH_6 has shown a striking catalytic role in the hydrogen sorption behavior. Xiao *et al.*³⁵ reported that the $\text{Mg}_2\text{FeH}_6@\text{MgH}_2$ core-shell sample exhibited faster hydrogen desorption kinetics, releasing more than 5.0 wt% H_2 within 50 min at 280 °C. Apart from the $\text{Mg}_2\text{FeH}_6-\text{MgH}_2$ system, Mg_2FeH_6 combined with NaBH_4 ³⁶ composite has boosted dehydrogenation properties, while the dehydrogenation temperature of NaBH_4 was reduced by at least 150 K when combined with Mg_2FeH_6 . The enhancement of the dehydrogenation properties of LiBH_4 was also confirmed by Li *et al.*³⁷ Mg_2FeH_6 is a hydrogen-storage material, which has an excellent ability for hydrogen uptake/release performance.³⁸ As an intermediate, Mg_2FeH_6 can uptake and liberate hydrogen. Therefore, the produced Mg_2FeH_6 plays a critical role in the improvement of the hydrogen storage properties.

The schematic diagram for the catalytic mechanism of Fe_7S_8 during the hydrogenation/dehydrogenation processes on MgH_2 is shown in Fig. 9. During the hydrogenation process, the phases of Fe, MgH_2 and H_2 are generated by the formation of the intermediate phase of Mg_2FeH_6 . In the dehydrogenation stage, Mg_2FeH_6 produces Mg and Fe. It is suggested that Fe as an active species exists in the whole dehydrogenation/hydrogenation process together with the newly formed MgS. Apart from that, from our previous investigation, the hydrogen absorption/desorption performance of the $\text{MgH}_2 + \text{Fe}$ and $\text{MgH}_2 + \text{MgS}$ systems is inferior to that of the *in situ* formed system.²⁹ Therefore, the newly produced Fe and MgS during the ball-milling stage may co-catalyze the hydrogen storage performance of the $\text{MgH}_2-\text{Fe}_7\text{S}_8$ system.

4. Conclusions

$\text{Nano-Fe}_7\text{S}_8$ was successfully fabricated and its catalytic effect on the hydrogen storage performance of MgH_2 was systematically investigated. The isothermal hydrogen absorption/desorption measurement shows that the dehydrogenated MgH_2 catalyzed by Fe_7S_8 composite has the hydrogen absorption capacity of 4.000 wt% within 1800 s at 473 K; only 1.847 wt% hydrogen could be absorbed by MgH_2 under the same conditions. During the dehydrogenation process, $\text{MgH}_2 + 16.7$ wt% Fe_7S_8 composite could release 4.403 wt% of hydrogen within 1800 s at 623 K as compared to 2.479 wt% of hydrogen by MgH_2 . The onset desorption temperature for Fe_7S_8 -modified MgH_2 is 420 K, lower than that of additive-free MgH_2 (710 K). The hydriding process of $\text{MgH}_2 + 16.7$ wt% Fe_7S_8 follows the nucleation and growth mechanism. The activation energy E_a of $\text{MgH}_2-\text{Fe}_7\text{S}_8$ is about 130.0 kJ mol⁻¹, approximately 36 kJ mol⁻¹ lower than that of MgH_2 . The striking catalytic effect of Fe_7S_8 on the hydrogen storage performance of MgH_2 is related to the reactions between MgH_2 and Fe_7S_8 . The newly formed MgS and Fe during the ball-milling process present a co-catalytic effect on the hydrogen storage performance of MgH_2 .

Conflicts of interest

There are no conflicts to declare.

Acknowledgements

This work was financially supported by the Natural Science Foundation of Hebei Province of China (No. E2019415036); Science and Technology Project of Hebei Education Department (BJ2020043); Science and Technology Support Plan of Qinhuangdao Science and Technology Bureau (201805A010); Doctoral Foundation of Hebei University of Environmental Engineering (201805).

Notes and references

- 1 Z. W. Ma, J. X. Zou, D. Khan, W. Zhu, C. Z. Hu, X. Q. Zeng and W. J. Ding, *J. Mater. Sci. Technol.*, 2019, **35**, 2132–2143.
- 2 M. Liu, S. Zhao, X. Xiao, M. Chen, C. Sun, Z. Yao, Z. Hu and L. Chen, *Nano Energy*, 2019, **61**, 540–549.
- 3 X. Xie, C. Ni, B. Wang, Y. Zhang, X. Zhao, L. Liu, B. Wang and W. Du, *J. Alloys Compd.*, 2020, **816**, 152634.
- 4 Z. Shao, Y. Li, C. Liu, W. Ai, S.-P. Luo and Q. Liu, *Nat. Commun.*, 2020, **11**, 591.
- 5 J. Du, Z. Lan, H. Zhang, S. Lu, H. Liu and J. Guo, *J. Alloys Compd.*, 2019, **802**, 660–667.
- 6 X. Yao, C. Wu, A. Du, J. Zou, Z. Zhu, P. Wang, H. Cheng, S. Smith and G. Lu, *J. Am. Chem. Soc.*, 2007, **129**, 15650–15654.
- 7 L. Dan, L. Hu, H. Wang and M. Zhu, *Int. J. Hydrogen Energy*, 2019, **44**, 29249–29254.
- 8 Z. Cao, L. Ouyang, H. Wang, J. Liu, L. Sun, M. Felderhoff and M. Zhu, *Int. J. Hydrogen Energy*, 2016, **41**, 11242–11253.



9 M. Liu, X. Xiao, S. Zhao, S. Saremi-Yarahmadi, M. Chen, J. Zheng, S. Li and L. Chen, *Int. J. Hydrogen Energy*, 2019, **44**, 1059–1069.

10 Y. Zheng, K. Li, H. Wang, D. Tian, Y. Wang, X. Zhu, Y. Wei, M. Zheng and Y. Luo, *Appl. Catal., B*, 2017, **202**, 51–63.

11 H.-J. Lin, J. Matsuda, H.-W. Li, M. Zhu and E. Akiba, *J. Alloys Compd.*, 2015, **645**, S392–S396.

12 G. Gizer, J. Puszkiel, M. V. C. Riglos, C. Pistidda, J. M. Ramallo-Lopez, M. Mizrahi, A. Santoru, T. Gemming, J. C. Tseng, T. Klassen and M. Dornheim, *Sci. Rep.*, 2020, **10**, 12.

13 G. Liang, J. Huot, S. Boily, A. V. Neste and R. Schulz, *J. Alloys Compd.*, 1999, **292**, 247–252.

14 M. Y. Song, S. N. Kwon, S. H. Hong, C. G. Park, S. H. Baek, H. S. Kim, D. R. Mumm and J. S. Bae, *Catal. Today*, 2007, **120**, 281–286.

15 S. Gao, X. Wang, H. Liu, T. He, Y. Wang, S. Li and M. Yan, *J. Power Sources*, 2019, **438**, 227006.

16 J. Zhang, L. He, Y. Yao, X. J. Zhou, L. P. Yu, X. Z. Lu and D. W. Zhou, *Renewable Energy*, 2020, **154**, 1229–1239.

17 F. A. H. Yap, N. N. Sulaiman and M. Ismail, *Int. J. Hydrogen Energy*, 2019, **44**, 30583–30590.

18 N. H. Idris, N. S. Mustafa and M. Ismail, *Int. J. Hydrogen Energy*, 2017, **42**, 21114–21120.

19 N. A. Ali, N. H. Idris, M. F. M. Din, N. S. Mustafa, N. A. Sazelee, F. A. H. Yap, N. N. Sulaiman, M. S. Yahya and M. Ismail, *RSC Adv.*, 2018, **8**, 15667–15674.

20 N. A. Sazelee, N. H. Idris, M. F. Md Din, M. S. Yahya, N. A. Ali and M. Ismail, *Results Phys.*, 2020, **16**, 102844.

21 M. Ismail, M. S. Yahya, N. A. Sazelee, N. A. Ali, F. A. H. Yap and N. S. Mustafa, *J. Magnes. Alloys*, 2020, **8**, 832–840.

22 T. B. Andres, M. Z. Luis and M. Marcos, *Int. J. Hydrogen Energy*, 2020, **45**, 27421–27433.

23 N. A. Ali, N. H. Idris, M. F. M. Din, M. S. Yahya and M. Ismail, *J. Alloys Compd.*, 2019, **796**, 279–286.

24 L. Zhang, L. Ji, Z. Yao, N. Yan, Z. Sun, X. Yang, X. Zhu, S. Hu and L. Chen, *Int. J. Hydrogen Energy*, 2019, **44**, 21955–21964.

25 D. M. Gattia, M. Jangir and I. P. Jain, *J. Alloys Compd.*, 2019, **801**, 188–191.

26 Y. Jia, S. Han, W. Zhang, X. Zhao, P. Sun, Y. Liu, H. Shi and J. Wang, *Int. J. Hydrogen Energy*, 2013, **38**, 2352–2356.

27 J. S. Wang, W. Zhang, Y. Cheng, D. D. Ke and S. M. Han, *J. Wuhan Univ. Technol., Mater. Sci. Ed.*, 2015, **30**, 670–673.

28 W. Zhang, Y. Cheng, D. Han and S. Han, *Energy*, 2015, **93**(pt 1), 625–630.

29 W. Zhang, G. Xu, Y. Cheng, L. J. Chen, Q. Huo and S. Y. Liu, *Dalton Trans.*, 2018, **47**, 5217–5225.

30 L. S. Xie, J. S. Li, T. B. Zhang and L. Song, *Mater. Charact.*, 2017, **133**, 94–101.

31 H. E. Kissinger, *Anal. Chem.*, 1957, **29**, 1702–1706.

32 J. S. Pedersen, *J. Appl. Crystallogr.*, 1994, **27**, 595–608.

33 L. Xie, Y. Liu, Y. T. Wang, J. Zheng and X. G. Li, *Acta Mater.*, 2007, **55**, 4585–4591.

34 R. A. Varin, T. Czujko, E. B. Wasmund and Z. S. Wronski, *J. Alloys Compd.*, 2007, **432**, 217–231.

35 X. Xiao, C. Xu, J. Shao, L. Zhang, T. Qin, S. Li, H. Ge, Q. Wang and L. Chen, *J. Mater. Chem. A*, 2015, **3**, 5517–5524.

36 G. Q. Li, M. Matsuo, S. Deledda, B. C. Hauback and S. Orimo, *Mater. Trans.*, 2014, **55**, 1141–1143.

37 G. Li, M. Matsuo, S. Deledda, R. Sato, B. Hauback and S.-I. Orimo, *Mater. Trans.*, 2013, **54**, 1532–1534.

38 Y. Wang, F. Cheng, C. Li, Z. Tao and J. Chen, *J. Alloys Compd.*, 2010, **508**, 554–558.

